# Anodic Dissolution Model Parameterization for Magnetically-Assisted Pulsed Electrochemical Machining (PECM)

C. Bradley

U.S. Army RDECOM-ARDEC, Benét Laboratories, Watervliet, NY 12189, USA

## Abstract

Electrochemical machining (ECM) is required for the manufacture of some complex micro-scale parts for biomedical devices and micro reactors that require an excellent surface finish. Additionally, the ECM current can be pulsed bidirectionally for bipolar pulsed ECM (PECM) to assist the electrochemical performance on passivated materials. The process can be further assisted with a magnetic field, where Lorentz forces can drive a magnetohydrodynamic (MHD) electrolyte flow. Modeling the effects of bipolar PECM in a magnetic field is a necessary first step to efficiently negotiating this complex parameter space with a comprehensive design methodology. The final workpiece geometry in this cell type is determined on a time scale much larger than the time scale over which the electrical pulses occur. These disparate time scales require a method for bridging them in a cohesive simulation. In the present work, cell average electrical conductivity and Faraday efficiency are chosen to parameterize machining performance for use in a finite element method model. Experiments used a 7075 aluminum workpiece in an NaNO3 electrolyte with a 316 stainless steel tool. The findings in this paper show the parameterization used in the magnetically assisted PECM model had an average error of 4%. Additional parameters are also proposed to capture higher fidelity morphology performance, evaluated against a novel XOR volume performance metric.

**Keywords:** Pulsed Electrochemical Machining (PECM), Morphology, Alpha Shape, Magnetically assisted

## Introduction

Non-conventional manufacturing processes such as electrochemical machining (ECM) has been required to manufacture complex micro-scale parts such as biomedical devices and micro reactors with an excellent surface finish from a wide range of specialty metals. ECM uses workpiece anodic dissolution in an electrolyte where the shape and proximity of a tool cathode partially determines the shape [1]. ECM can be assisted by pulsing the current between the electrodes [2]. Reverse polarity pulses can be added making the pulsed electrochemical machining (PECM) bipolar, further assisting the performance of the process by removing passivation layers to increase surface quality and efficiency [3, 4, 5, 6, 7].

PECM relies on an electrolyte to transfer machining energy to the workpiece where there are electrochemical and fluid interactions that play a significant role in process performance [8]. The literature on ECM discusses pulsed electric fields that improve conductivity and as a result an increase in machining performance in terms of material removal rate (MRR) [9, 10]. Magnetic fields are another way to assist ECM performance [8, 11]. Magnetic fields increase the Lorentz force on the electrolyte in the inter-electrode gap (IEG), increasing electrolyte flow. This flow can then increase conductivity and efficiency to improve ECM performance in terms of MRR [12, 13, 14]. Both assistances, PECM and magnetic fields, can be combined for a dual-assisted anodic-dissolution process that further increases performance [15, 16, 17]. This dual-assisted ECM will generate a complex magnetohydrodynamic (MHD) electrolyte flow, where the electromagnetics are coupled with the fluid dynamics.

In the case of PECM on-times are typically much smaller than the total machining time they are used over. To study large time scale effects caused by small time scale events the effects must be bridged from the smaller up to the larger. Studies in the literature have considered empirical modeling methods of PECM in terms of peak current and efficiency [2]. Idrisov et al. [18] used a 1D simulation of bipolar PECM to predict a theoretical \localization factor" as a measure of accuracy based on current over a large time scale. Additionally, Weber et al. [19] used electrochemical impedance spectroscopy (EIS) and the Fourier transform to convert current pulses to an exponential function in order to predict steady-state PECM current in a large time scale numerical model. Numerical finite element method (FEM) models have also been used to simulate the PECM current from one pulse for a small time scale model [20]. Feng et al. [21] simulated MRR in PECM by averaging a 3 kHz pulse so that it could be used in a large time scale model. Chen et al. [22] assumed a quasi-steady state using current averaging to simulate MRR with respect to IEG temperature. EIS has also been used to determine

conductivity for a hydrodynamic flow model over a small time scale in a PECM cell [23].

In the case of magnetically assisted electrochemical cells several methods have been used in time dependent models over a large time scale. Empirical and analytic models have been developed for current on a steady state electrode in magnetically assisted, reversible electrochemical cells, but those cell types are not necessarily representative of non-reversible PECM [24, 12]. Empirical models specific to magnetically assisted ECM have also been studied in relation to accuracy [13, 14]. While another empirical model presented a characterization of magnetically assisted PECM, based on waveform phase difference [17]. Additionally, there is one magnetically assisted ECM model of MRR on a large time scale that studied turbulent MHD electrolyte flow under different magnetic field orientations [25]. While the cited studies may consider PECM performance or magnetically assisted ECM it was either not concurrent or did not address MRR.

Considering the above state-of-the-literature, this paper proposes a parameterization of a magnetically assisted PECM cell to capture MRR performance in a numerical simulation. This parameterization helps to capture the small time scale effects for use in a large time scale model of anodic dissolution (AD). The average simulation results of MRR are within 4% of the experimental results. Additionally, the effect of a surface current limit is investigated in an effort to capture higher fidelity morphology performance.

The remainder of the paper is structured as follows. Section 2 and Section 3 discuss the theory and experiment details respectively. Section 4 presents the details of the numerical model, while Section 5 outlines the results. Finally, section 6 outlines the specific conclusions that can be drawn from this study.

## Theory

The time averaged parameters for conductivity ($Y_{ave}$) and current efficiency ($\theta$) aggregates the small time scale effects of PECM frequency coupled with the magnetic field over the large time scale of the total machining time, $t_{final}$. By averaging these cell parameters a DC ECM simulation can simulate a magnetically assisted PECM cell. This is possible because the definition of Faraday's Laws rely on the total charge, Q, passing through the workpiece, which is the integral of the current, I,

$$Q = \int_0^{t_{final}} I\,dt = \int_0^{t_{final}} Y_{ave} \cdot V\,dt. \quad (1)$$

Faraday's laws of electrolysis determine the mass of material removed per unit charge d Faraday's laws of electrolysis determines the mass of material removed per unit charge during the cell reaction. The additional term, , in Eq. 2 is the experimentally derived cell efficiency and can be calculated as the ratio of actual mass removed in an experiment divided by the theoretical mass predicted by Faraday's laws of electrolysis summarized by,

$$m_{pred} = \theta\ \left(\frac{Q}{F}\right)\left(\frac{M_{eqv}}{z_{eqv}}\right), \quad (2)$$

where the predicted mass removed of the equivalent alloy is m, machining electrical, Q, Faraday's constant, $F$, alloy molar mass, $M_{eqv}$, and $z_{eqv}$ is the alloy ion valency [26, 27].

So by combining a small time scale measurement of average conductivity over a PECM pulse and a large time scale measurement of cell efficiency a time dependent simulation of AD will capture the volume and by extension the MRR performance according to Eqns. 1 and 2. That allows the MRR of a given cell with a certain set of conditions to be characterized by the parameters $Y_{ave}$ and $\theta$. This characterization assumes the secondary current distribution is not dominated by ion concentration.

Model fidelity can be investigated for a wider range of problems if a secondary current distribution is considered that takes electrolyte concentration into account. While this should not impact MRR for typical concentrations considered in this work the concentration dependence can significantly change the morphology of the machined surface. Alloy cation concentration was used to define electrode kinetics based on their convection and diffusion, allowing simulations to be run over a range of current limits. The effect of the current limit on the machined hole morphology requires the evaluation of a performance metric that captures differences in surface shape in a mathematically bounded manner.

The morphology metric used to quantify simulation error in this current study is the alpha shape of the simulated hole surface combined with the scan of the experimental hole. When the two surfaces are combined using the alpha shape function the new volume forms the XOR of the two hole volumes. The XOR volume can then be divided by the total scanned hole volume and is a robust measure that quantifies morphological error [28, 29].

## Experimental Design

The experimental study used a 316 stainless steel tool (cathode) and a flat 7075 aluminum alloy workpiece (anode). Table 1 lists the aluminum alloy composition

commonly used in the aerospace industry [30]. The non-ferromagnetic cathode and anode do not interact with the magnetic field, allowing a more consistent field that can be measured offline from the assembled flow cell [31].

**Table 1:** Summary of experimental conditions

| Workpiece | 7075 aluminum, 3.175 mm diameter, Al 89.3%, Cu 1.6%, Mg 25%, Other 1.0%, Zn 5.6% |
|---|---|
| Tool | 316 stainless steel 1.5 mm diameter, insulated diameter |
| Magnetic Field | • Flux Density ($B$): 370 mT |
| Process | • $NaNO_3$ Mass Concentration: 20%<br>• Temperature: 21-23C<br>• Inter-electrode Gap: 110 μm<br>• Electrolyte Flow: 116-125 ml/min<br>• Machining Time ($t_{final}$): 15 s<br>• Average Conductivity ($Y_{ave}$): S<br>• Efficiency ($\theta$): % |
| Voltage Pulse | • Voltage ($V$): +6:5, -5 V<br>• Frequency ($f$): 4000 Hz<br>• Duty Cycle: 50% anodic, 20% delay, 2% cathodic |
| Output | • Total Volume Error ($Vol_{err}$): %<br>• Alpha Volume Error ($\alpha_{err}$): % |

The constant magnetic field is shown in Fig. 1 with labels indicating the tool and workpiece diameters. Magnetic flux density is measured in the "Y" direction from one permanent magnet North pole to the opposite magnet South pole. The consistency of the field is seen in that the range of the flux density is only 6% of the mean and much more consistent within the IEG defined by the tool diameter. The flow cell is shown in Fig. 2 with the major components noted.

The flow cell, workpiece seals, and magnet brackets are 3D printed. By using position indicators printed into the flow cell and magnet brackets the magnets are positioned precisely and consistently and this in turn controls the magnetic flux density.

## Numerical Model

The AD model output is the deformed surface. The total volume removed during a simulation is calculated as the integral of the "Z" deformation of the surface seen in Fig. 3. The current density overlaid on the deformed mesh surface in Fig. 3 also shows the current flow noted by the vertical "yellow" arrow and the
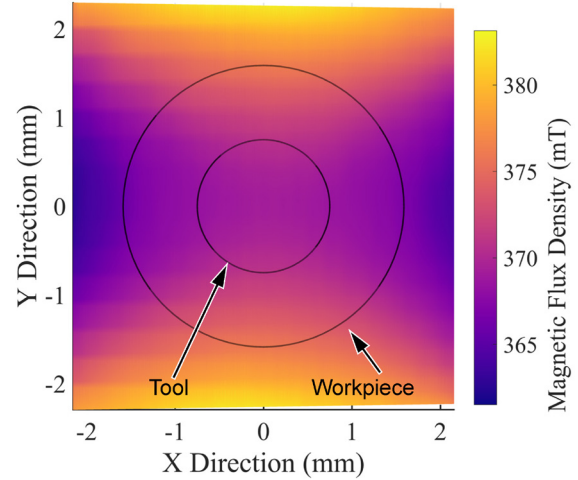


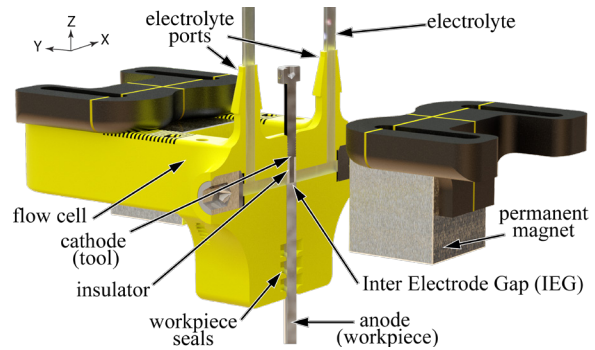**Figure 1**. Magnetic field flux density map in the "Y" direction from one magnet face to the other



**Figure 2**. Partial cutaway of experimental flow cell model with permanent magnets

direction of electrolyte flow noted by a "blue" arrow along the "X" axis. All simulations were conducted in COMSOL 5.2® using the electrochemistry, deformed geometry, and the transport of diluted species modules to solve the secondary current distribution, mesh deformation, and the alloy ion convection-diffusion equations respectively.
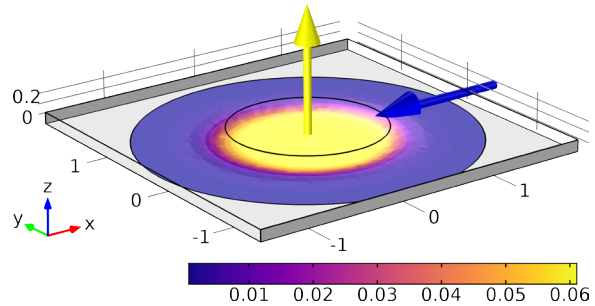


**Figure 3**. Surface current density on workpiece

The AD model uses the parallel direct solver (PARDISO) for the secondary electrode current distribution simulation simultaneously with the other
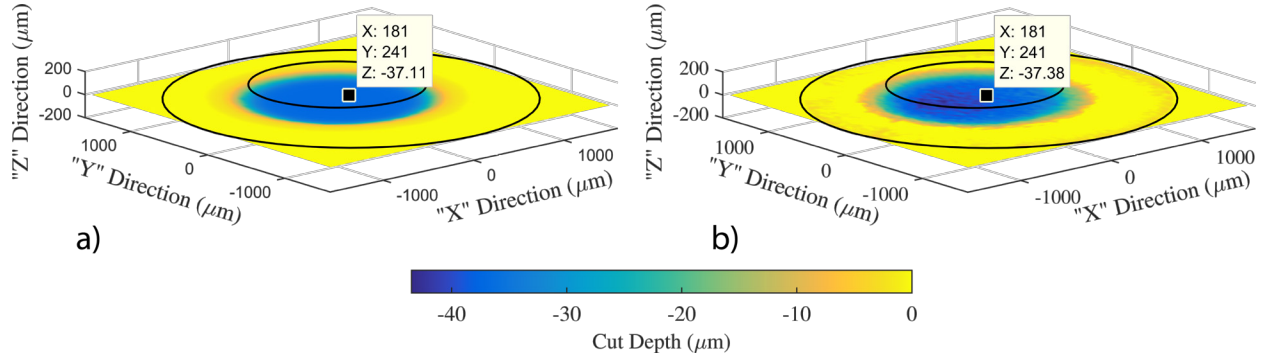
**Figure 4:** Workpiece surface depth from starting datum (a) simulation of deformed mesh surface, (b) surface scan of workpiece from experiment

physics modules [32]. PARDISO is also used to solve the convection-diffusion equation for alloy ions concentration as well as account for mesh deformation. This current distribution is the primary driver of anodic dissolution over time based on alloy density, molar mass, and Faraday's laws of electrolysis from Eq. 2.

The simulation begins with a stationary simulation step to set initial conditions for electrical current and ion concentration. Each time-varying simulation step is fully coupled and includes current, deformation, and ion concentration. Workpiece dissolution is mimicked by deforming the mesh over time using the arbitrary Lagrangian-Eulerian (ALE) method driven by current density that is also a function of ion concentration. A deformed mesh is compared to a surface scan from an experimental conducted under the same cell conditions in Fig. 4a and b. The simulation yields a deformed surface that can be directly compared to an experimental surface.

The surface data is then exported via an "STL" file format to perform computational geometry calculations in MATLAB®. The surface integral of the "Z" depth is used as the measure of material removed during machining. This integral calculation is a standard method for determining volume.

To assess the morphological difference between a hole machined in simulation and one from an experiment the alpha shape function is used to define a bounding region. The volume of this bounding region is representative of the morphological difference. The alpha shape is a generalization of the convex hull [33]. The convex hull is the intersection of all convex sets containing a finite set of points. A convenient way to describe the convex hull is the shape created by a rubber band stretched around a set of points. The alpha shape is then the shape created when a circle defined by a radius presses into the convex hull rubber band shape without passing through any points. As that radius goes to infinity the alpha shape becomes the convex

hull. All alpha shape calculations used a radius of 10 μm. When the alpha shape function is applied to the points that represent both the simulated and experimental surfaces the result is the logical exclusive "or" function of the two volumes or XOR. If two surfaces overlap exactly then the XOR of the points tends toward zero.

## Results and Discussion

Two experiments were run under the same conditions and then simulations were run based on measurements of $Y_{ave}$ and $\theta$, over a range of surface current limits from 0.065 to 0.090 $\frac{A}{mm^2}$. All other process parameters were held constant.

The machined hole was measured using a structured light surface scanner. The total volume error, $Vol_{err}$, for the two experiments had a mean of 4% and a one standard deviation error bar at 6%, regardless of surface current limit. This indicates the volume and MRR are well parameterized by $Y_{ave}$ and $\theta$. The total volume error, $Vol_{err}$, for the simulations is shown in the circumscribed bar graph in Fig. 6.



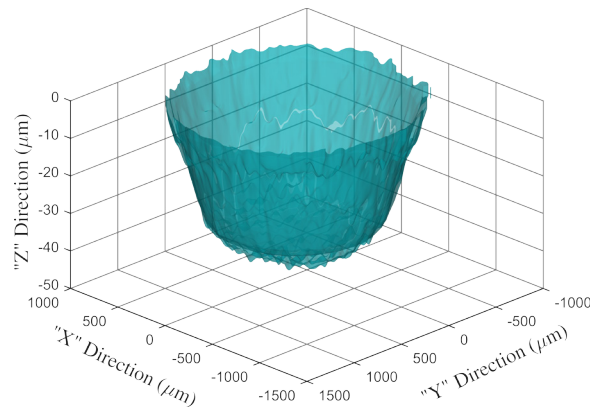**Figure 5.** Alpha shape function representing the volume XOR comparing one experimental run to one simulation at a current limit of 0.08 $\frac{A}{mm^2}$.

Separately, the alpha shape combines the simulated hole from Fig. 4a and experimental hole scan in Fig. 4b. The XOR volume as calculated using the alpha shape function and is shown in Fig. 5 with transparency to show surface texture. When the XOR volume is divided by the total experimental hole volume it quantifies morphological simulation error and is robust when scan points differ significantly from the simulation mesh in resolution or alignment. The best error at one standard deviation in Fig. 6 is at a surface current limit of 0.08 $\frac{\text{A}}{\text{mm}^2}$ with an error of 9%. The alpha error, $\alpha_{\text{err}}$, is shown in the surrounding bar graph in Fig. 6. The total volume was near constant, independent of the current limit, whereas the morphology is highly affected by the current limit, seen in Fig. 6.
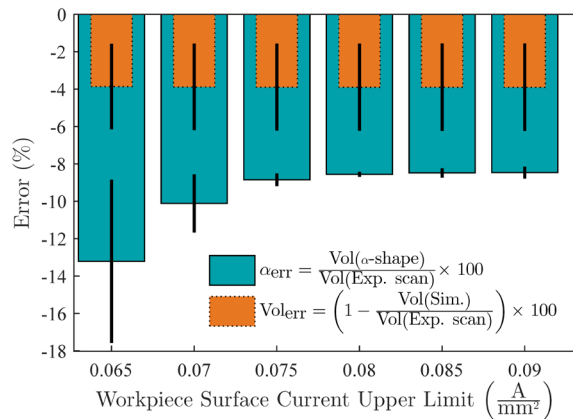


**Figure 6**. Total volume error, Vol$_{\text{err}}$, as a function of surface current limit shown in circumscribed bar graph with alpha volume error, $\alpha_{\text{err}}$, comparing morphology shown in surrounding bar graph

## Conclusion

By parameterizing machining performance the total volume and MRR can be accurately simulated from a measured $Y_{\text{ave}}$ and $\theta$. However, the morphology requires additional measures to parameterize the machining conditions including the current limit and possibly other parameters. The machining environment parameters of magnetic field flux density and PECM frequency interact in a complex manner that is difficult to directly simulate, but total volume is well characterized using $Y_{\text{ave}}$ and $\theta$. This has the potential to simplify the design process when navigating and optimizing within the complex design space. Conceivably, a design methodology based on this parameterization could allow extrapolation and prediction in the design space of magnetically assisted PECM.

## References

[1] F. Pitschke, General applications of electrochemical machining, Tech. Rep. 620205, *SAE Technical Paper*, Troy, MI, USA (1962)

[2] M. Datta, D. Landolt, Electrochemical machining under pulsed current conditions, *Electrochimica Acta* 26 (7) (1981) 899-907

[3] T. Masuzawa, M. Kimura, Electrochemical surface finishing of tungsten carbide alloy, *CIRP Annals* 40 (1) (1991) 199-202.

[4] C. Zhou, E. Taylor, J. Sun, L. Gebhart, E. Stortz, R. Renz, Electrochemical machining of hard passive alloys with pulse reverse current, *Transactions-North American Manufacturing Research Institute of SME* 25 (1997) 147-152.

[5] A. Zaytsev, I. Agafonov, N. Gimaev, R. Moukhoutdinov, A. Belogorsky, Precise pulse electrochemical machining by bipolar current: Aspects of effective technological application, *Journal of Materials Processing Technology* 149 (1) (2004) 419-425.

[6] R. Mathew, M. M. Sundaram, Modeling and fabrication of micro tools by pulsed electrochemical machining, *Journal of Materials Processing Technology* 212 (7) (2012) 1567-1572.

[7] W. Natsu, D. Kurahata, Observation of workpiece surface in ecm process of wc alloy micropin with bipolar pulses, *International Journal of Electrical Machining* 21 (0) (2016) 31-38.

[8] P. B. Tailor, A. Agrawal, S. S. Joshi, Evolution of electrochemical finishing processes through cross innovations and modeling, *International Journal of Machine Tools and Manufacture* 66 (2013) 15-36.

[9] M. Inman, T. Hall, E. Taylor, C. Reece, O. Trofimova, Niobium electropolishing in an aqueous, non-viscous hf-free electrolyte: A new polishing mechanism, in: *Proceedings of SRF2011*, Chicago, IL, (2011), 377-381.

[10] J. W. Park, D. W. Lee, Pulse electrochemical polishing for micro recesses based on a coulostatic analysis, *The International Journal of Advanced Manufacturing Technology* 40 (7-8) (2009) 742-748.

[11] J. Fang, Z. Jin, W. Xu, Y. Shi, Magnetic electrochemical finishing machining, *Journal of Materials Processing Technology* 129 (1-3) (2002) 283-287.

[12] O. Lioubashevski, E. Katz, I. Willner, Magnetic field effects on electrochemical processes: A theoretical hydrodynamic model, *The Journal of Physical Chemistry B* 108 (18) (2004) 5778-5784.

[13] Z. Fan, T. Wang, L. Zhong, The mechanism of improving machining accuracy of ecm by magnetic field, *Journal of Materials Processing Technology* 149 (2004) 409-413.

[14] L. Tang, W. Gan, Experiment and simulation study on concentrated magnetic field-assisted ECM S-03 special stainless steel complex cavity, *The International Journal of Advanced Manufacturing Technology* 72 (5-8) (2014) 685-692.

[15] P. Pa, Mechanism design of magnetic-assistance in surface finishing of end-turning, *Journal of Advanced Mechanical Design Systems and Manufacturing* 2 (4) (2008) 587-596.

[16] L. Yin, W.-m. Zhang, Y. Yan, Q.-s. Tu, Z.-j. Zhang, Study of electrochemical finishing with magnetic field and high-frequency group pulse, in: 2010 *International Conference on Digital Manufacturing & Automation*, Vol. 2, (2010), 440-443.

[17] C. Bradley, J. Samuel, Controlled phase interactions between pulsed electric fields, ultrasonic motion, and magnetic fields in an anodic dissolution cell, *Journal of Manufacturing Science and Engineering* 140 (4) (2018) 041010-1-041010-10.

[18] T. Idrisov, A. Zaitzev, V. Zhitnikov, Estimation of the process localization at the electrochemical machining by microsecond pulses of bipolar current, *Journal of Materials Processing Technology* 149 (1-3) (2004) 479-485.

[19] O. Weber, H. Natter, D. Bähre, Pulse electrochemical machining of cast iron: A Layer based approach for modeling the steady-state dissolution current, *Journal of Solid State Electrochemistry* 19 (5) (2015) 1265-1276.

[20] O. Weber, A. Rebschläger, P. Steuer, D. Bähre, Modeling of the material/electrolyte interface and the electrical current generated during the pulse electrochemical machining of grey cast iron, in: *Proceedings of the European COMSOL Conference*, (2013), 1-6.

[21] W. Feng, Z. Jianshe, Z. Xiangli, Y. Zhenwen, G. Weimin, T. Zongjun, Electrochemical machining of a narrow slit by cathodic compound feeding, The

International Journal of Advanced Manufacturing Technology 90 (1-4) (2017) 971-978.

[22] Y. Chen, M. Fang, L. Jiang, Multiphysics simulation of the material removal process in pulse electrochemical machining (PECM), *The International Journal of Advanced Manufacturing Technology* 91 (5-8) (2017) 2455-2464.

[23] C. Bradley, J. Samuel, Magnetohydrodynamic electrolyte flow within an inter-electrode gap driven by a sinusoidal electric field and constant magnetic field, in: *COMSOL Multiphysics Conference*, Boston, MA, (2017) 1-7.

[24] O. Aaboubi, Magnetic field effects on mass transport, *Journal of The Electrochemical Society* 137 (6) (1990) 1796-1804.

[25] L. Long, M. Baoji, W. Ruifeng, D. Lingqi, The coupled effect of magnetic field, electric field, and electrolyte motion on the material removal amount in electrochemical machining, *The International Journal of Advanced Manufacturing Technology* 91 (9-12) (2017) 2995-3006.

[26] R. A. Serway, C. J. Moses, C. A. Moyer, *Modern Physics*, Cengage Learning, Belmont, CA, USA, (2004).

[27] S. Mukherjee, S. Kumar, P. Srivastava, A. Kumar, Effect of valency on material removal rate in electrochemical machining of aluminium, *Journal of Materials Processing Technology* 202 (1-3) (2008) 398-401.

[28] X. Jiang, S. Lou, P. J. Scott, Morphological method for surface metrology and dimensional metrology based on the alpha shape, *Measurement Science and Technology* 23 (1) (2012) 015003.

[29] S. Lou, X. Jiang, P. J. Scott, Algorithms for morphological profile filters and their comparison, *Precision Engineering* 36 (3) (2012) 414-423.

[30] R. S. Shevell, *Fundamentals of Flight*, Prentice-Hall, Englewood Cliffs, NJ, USA, (1983).

[31] A. Tavassoli, Assessment of austenitic stainless steels, *Fusion Engineering and Design* 29 (1995) 371-390.

[32] N. P. Aryan, H. Kaim, A. Rothermel, Primary current distribution and electrode geometry, in: *Stimulation and Recording Electrodes for Neural*

*Prostheses*, Vol. 78, Springer, New York, NY, USA, (2015), 25-30.

[33] H. Edelsbrunner, D. Kirkpatrick, R. Seidel, On the shape of a set of points in the plane, *IEEE Transactions on information theory* 29 (4) (1983) 551-559.